ACS APPLIED MATERIALS & INTERFACES

www.acsami.org

Research Article

ZnS Ultrathin Interfacial Layers for Optimizing Carrier Management in Sb_2S_3-based Photovoltaics

Pascal Büttner, Florian Scheler, Craig Pointer, Dirk Döhler, Tadahiro Yokosawa, Erdmann Spiecker, Pablo P. Boix, Elizabeth R. Young,* Ignacio Mínguez-Bacho,* and Julien Bachmann*

Cite This: *ACS Appl. Mater. Interfaces* 2021, 13, 11861−11868

Read Online

ACCESS | Metrics & More | Article Recommendations | Supporting Information

ABSTRACT: Antimony chalcogenides represent a family of materials of low toxicity and relative abundance, with a high potential for future sustainable solar energy conversion technology. However, solar cells based on antimony chalcogenides present open-circuit voltage losses that limit their efficiencies. These losses are attributed to several recombination mechanisms, with interfacial recombination being considered as one of the dominant processes. In this work, we exploit atomic layer deposition (ALD) to grow a series of ultrathin ZnS interfacial layers at the TiO_2/Sb_2S_3 interface to mitigate interfacial recombination and to increase the carrier lifetime. ALD allows for very accurate control over the ZnS interlayer thickness on the ångström scale (0−1.5 nm) and to deposit highly pure Sb_2S_3. Our systematic study of the photovoltaic and optoelectronic properties of these devices by impedance spectroscopy and transient absorption concludes that the optimum ZnS interlayer thickness of 1.0 nm achieves the best balance between the beneficial effect of an increased recombination resistance at the interface and the deleterious barrier behavior of the wide-bandgap semiconductor ZnS. This optimization allows us to reach an overall power conversion efficiency of 5.09% in planar configuration.

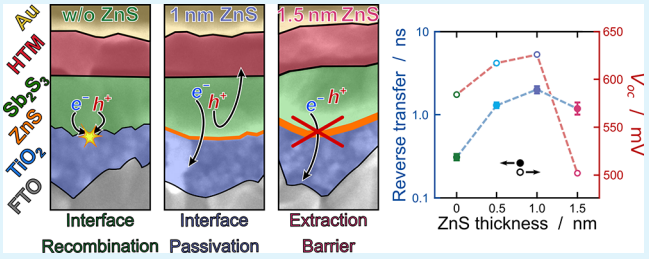

KEYWORDS: *tunnel barrier, interfacial layer, passivation layer, anti-recombination layer, chalcogenides, extremely thin absorber, thin film solar cells, atomic layer deposition*

INTRODUCTION

The application of earth-abundant materials with low toxicity to solar energy conversion devices would enable mass deployment of sustainable technologies. Established thin film solar cell technologies, based on materials such as CdTe and $Cu(In,Ga)(S,Se)_2$ (CIGS), have achieved efficiencies of 22.1% and 23.35%, respectively.[1] Perovskite solar cells, the flagship of the so-called emerging photovoltaics, have even reached efficiencies of more than 25.5%.[1] These outstanding efficiencies position those technologies at similar performance level as traditional crystalline silicon solar cells.[1] Nevertheless, either scarcity or toxicity concerns of the materials composing the heterojunctions represent a significant hurdle for them to be considered as a competitive alternative to silicon-based solar panels. In that sense, $Cu_2ZnSn(S,Se)_4$ (CZTS) has been considered as one of the most promising materials for potential mass deployment, and the current record high efficiency of photovoltaic junctions based on it is 12.6%.[2] However, the quaternary nature of kesterites generates a complex system of secondary phases that is difficult to control and limits their potential to reach competitive efficiencies. Therefore, materials of simpler compositions represent an important pathway to investigate. In particular, antimony chalcogenides have recently attracted significant attention in the thin-film PV community.[3−8] This family of materials is based on simple binary structures, it features high absorption coefficients $\alpha > 5 \times 10^4$ cm^{-1}, and presents the possibility to tune the bandgap (1.1−1.7 eV).[7] However, photoconversion efficiencies of solar cells based on antimony chalcogenides are still far from the Shockley-Queisser limit.[9] Yet, they are expected to improve further in the foreseeable future.[10] To date, the achievable efficiencies of antimony chalcogenides solar cells are largely held back by an open circuit voltage (V_{oc}) deficit of ∼0.5−0.6 eV, for which self-trapped photoexcited carriers, defects in the bulk, and interfacial trap states have been considered as causes.[3,10,11] Insight into the dynamics of charge carriers in these systems has been provided by impedance spectroscopy and ultrafast optical methods, which allow one to cover time scales ranging from femtoseconds to seconds.[6,11−14] Ultrafast self-trapping of excitons in antimony chalcogenides, and in particular of Sb_2S_3, has been ascribed to the partly one-

Received: December 3, 2020
Accepted: February 25, 2021
Published: March 5, 2021

dimensional nature of the crystal and would set an intrinsic limitation for this family of materials.[6,15,16] A completely distinct effect, however, has been pointed out as the dominant limitation, namely the recombination of photogenerated carriers at interface traps.[8,17,18] In particular, the interface of Sb_2S_3 with TiO_2 presents positively charged vacancies whith trap states below the conduction band.[19] Thus, any improvement in the quality of this interface should represent an immediate performance enhancement of the corresponding photovoltaic device by improving the carrier transfer to the electron and hole transport materials. To this end, various interlayers have been proposed.[20−24] One material that has been considered in other chalcogenide solar cells, in particular as a nontoxic and more transparent alternative to CdS for buffer layers, is ZnS (or zinc oxysulfide). In the present work, we utilize atomic layer deposition (ALD) to deposit not only a highly pure Sb_2S_3 light absorber layer, but also an ultrathin interfacial layer of ZnS between it and TiO_2. This layer serves a double purpose. First, it resolves the chemical incompatibility between TiO_2 and Sb_2S_3 and generates a stable, adhesive interface. Second, it passivates interface trap states and inhibits the deleterious reverse transfer of electrons from the oxide into Sb_2S_3.[25] Its nature as a tunnel barrier, however, inherently means that the device performance must depend on the interlayer thickness in a highly sensitive manner. To address this aspect, ALD is uniquely suited since it allows for an experimental control of the thickness on the ångström scale, including for nonplanar substrates.[26] Here, we adjust the nominal thickness of the ZnS interfacial layer between 0 and approximately 1.5 nm by performing 0 to 15 ALD cyclces and we investigate the morphology of the ZnS interlayer by high-resolution transmission electron microscopy (HRTEM). We systematically evaluate the physical characteristics of the semiconductor heterojunction, as they depend on the ZnS thickness, and are able to decipher how the dominant physical limitation of the junction changes as the interlayer is grown beyond 1.0 nm.

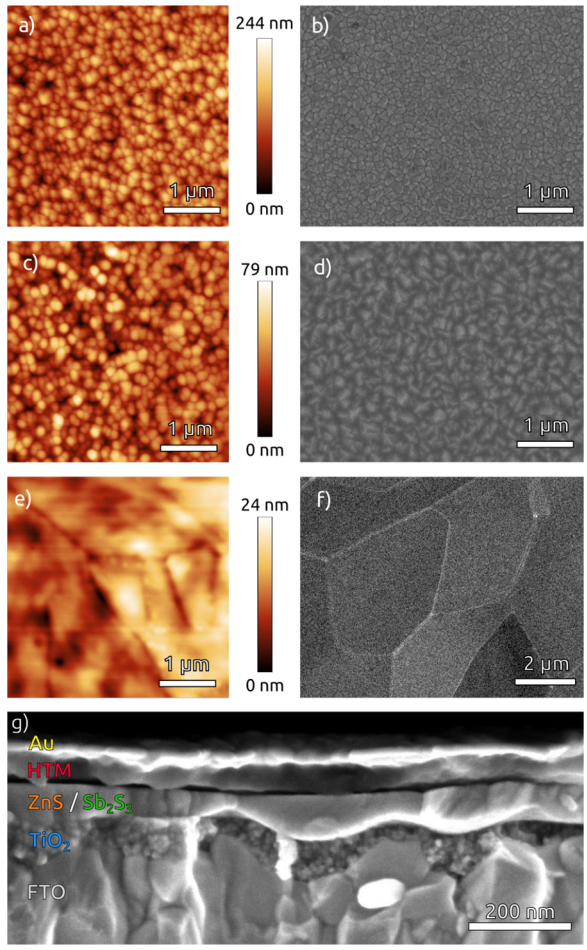

Figure 1. AFM and SEM micrographs of (a, b) FTO, (c, d) TiO_2 spin-coated on FTO, and (e, f) Sb_2S_3 deposited via ALD on FTO/TiO_2, after annealing. The RMS roughness of the respecive layers are 29, 13 and 3 nm, respectively; (g) SEM micrograph of a complete device in cross-section view.

RESULTS AND DISCUSSION

Device Structure. In this study, we consider an n-i-p structure that is commonly employed in thin film solar cells and has demonstrated high performances for Sb_2S_3-based solar cells. In the first preparatory step, a compact layer of TiO_2 is spin-coated on the fluorine-doped tin oxide (FTO) substrate to serve as the electron transport material (ETM). Spin-coating enables reduction of the initial surface roughness, as demonstrated by atomic force microscopy (AFM). In Figure 1a,b, the root-mean-square (RMS) roughness of FTO is estimated at 29 nm, whereas after the TiO_2 coating it is reduced to 13 nm (Figure 1c,d). In the subsequent step, ALD is used to deposit pinhole-free thin layers of ZnS and Sb_2S_3 with nearly perfect conformality.[26] The ZnS interlayer is varied in a series of samples with 0 to 15 ALD cycles, corresponding to approximately 0−1.5 nm. Subsequently, the light-absorbing Sb_2S_3 layer (75 nm) is added by ALD in the same vacuum (i.e., without opening the chamber). The initially conformal morphology of the as-grown, amorphous Sb_2S_3 material changes upon conversion to the stibnite phase during annealing. This thermal treatment results in the formation of large stibnite grains and simultaneously smooths out the surface. At this stage, the AFM investigation yields an RMS roughness of 3 nm only, whereas grains with a lateral size of several micrometres are apparent in scanning electron microscopy (SEM), Figure 1e,f. The lateral stibnite grain size vastly exceeds the film thickness (75 nm) of the absorber layer, which means that no grain boundaries can compromise charge carrier extraction within the Sb_2S_3 thin film to any significant degree. In the final steps of preparation, poly(3-hexylthiophene-2,5-diyl) (P3HT) and poly(3,4-ethylenedioxythiophene) polystyrenesulfonate (PEDOT:PSS) are added as the hole transport materials (HTM) and gold is evaporated for electrical contacts. The final device cross-section is presented in Figure 1g.

The ultrathin ZnS layer between the oxide and annealed Sb_2S_3 is clearly observable in high-resolution transmission electron microscopy (HRTEM, Figure 2a). Its small, randomly oriented crystalline particles are visible in real space and fast-Fourier transform (FFT) from the TEM images (Figure 2b), distinct from the very large Sb_2S_3 crystals. The FFT of the ZnS nanocrystals reveals an interplanar *d*-spacing of 0.19 and 0.16 nm, corresponding to the $(2\bar{2}0)$ and $(31\bar{1})$ planes of the zinc blende structure of ZnS. We note that ZnS behaves similarly on crystalline TiO_2, amorphous TiO_2, and on amorphous SiO_2. HRTEM shows a single crystal region of the Sb_2S_3 with interplanar *d*-spacing of 0.17 nm corresponding to the (321) plane. Energy-dispersive X-ray spectroscopy mapping images

https://dx.doi.org/10.1021/acsami.0c21365
ACS Appl. Mater. Interfaces 2021, 13, 11861−11868

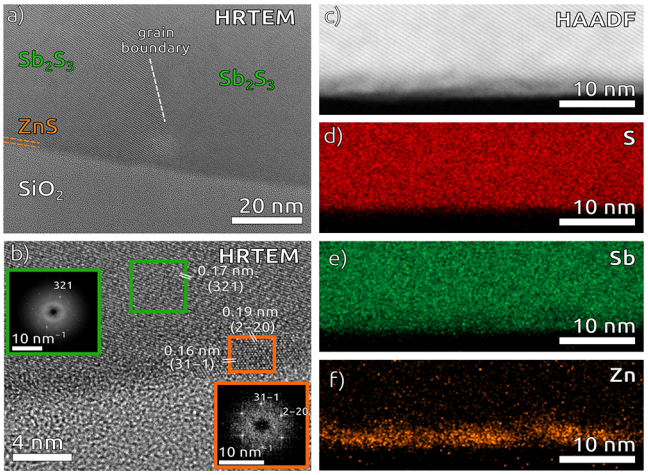

Figure 2. (a) HRTEM image of the Sb_2S_3/ZnS interface grown on a silicon wafer. (b) Higher magnification with the corresponding FFTs of the Sb_2S_3 layer (green frames) and the ZnS interlayer (oragen frames) as insets. (c) High-angle annular dark field (HAADF) and (d−f) STEM-EDX mapping images displaying the elemental distribution of (d) S, (e) Sb and (f) Zn.

based on scanning TEM (STEM-EDX) confirm that ZnS has not diffused into Sb_2S_3 (Figure 2c−f).

Device Performance. The introduction of the ZnS interlayer, even with a thickness of only a few ångströms, has a significant impact on the device performance. Figure 3a,b reveals that the beneficial effect of this layer is optimized in a reproducible manner for a thickness of 0.5 to 1.0 nm. Specifically, it increases the average device efficiency from 3.5% for ZnS-free devices to above 4.0% (Figure 3b). This improvement is mostly associated with a significant increase of the average V_{oc} from 554 mV to 609 mV for solar cells with 5 cycles of ZnS (SI Figure S1a of the Supporting Information, SI). Devices with 15 cycles of ZnS exhibit a dramatic drop of all device performance parameters. This is shown by external quantum efficiency (EQE) spectras (Figure 3c) for the J_{sc}, which collapses when 1.5 nm ZnS is present, whereas below 1.0 nm, the effect of a thin interfacial layer is moderate and monotonous. Table 1 shows a summary of the best performing devices for each ZnS thickness. The dark *JV*-curves show a significant improvement of the blocking behavior of the n-i-p diode structure. A 0.5 nm portion of ZnS already suffices to deliver a significant beneficial effect, which is further augmented with 1 nm of ZnS (Figure 3d). However, the detrimental effect of the series resistance, R_s, becomes evident and takes over for 1.5 nm ZnS. The effect of ZnS as a "thick" layer is in line with expectations based on the band structure of the TiO_2/ZnS/Sb_2S_3 heterojunction. The large bandgap of ZnS (3.55 eV)[27] and its high conduction band offset with respect to both TiO_2 and Sb_2S_3 result in the formation of a tunneling barrier for negative carriers. Thus, the behavior of the 1.5 nm thick layer is in line with the exponential decay of the tunneling probability as a function of the barrier width.

Table 1. Summary of the Best Performing Devices for Each ZnS Thickness

ZnS thickness (nm)	V_{oc} (mV)	J_{sc} (mA cm^{-2})	FF	efficiency (%)
0	584	14.4	0.51	4.32
0.2	554	15.5	0.47	4.05
0.5	617	15.8	0.49	4.73
1.0	626	15.7	0.52	5.09
1.5	502	8.5	0.34	1.43

Physical Investigation. Further insight into the physical processes at work at the interface is provided by impedance spectroscopy. Data sets recorded under 1 sun illumination and

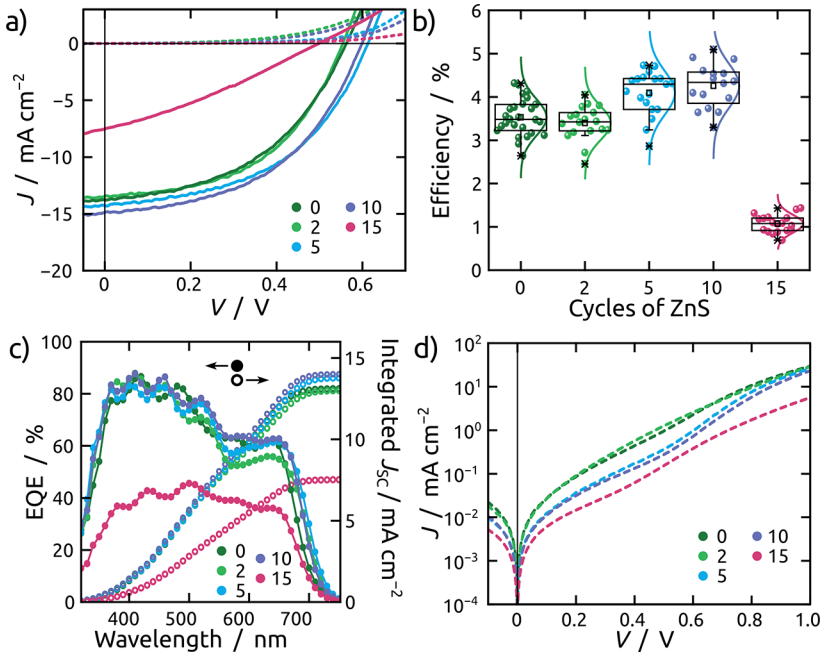

Figure 3. Effect of ZnS thickness on device performance. (a) Representative *JV*-curves for each ZnS thickness under 1.0 sun illumination (solid lines) and in the dark (dashed lines). (b) Statistics of device efficiencies with error bars. (c) Corresponding EQE spectra (filled symbols) with photocurrent integration over the visible spectrum (hollow symbols). (d) Logarithmic plot of the dark *JV*-curves. Statistics on V_{oc}, J_{sc}, and FF can be found in the SI (Figure S1).

https://dx.doi.org/10.1021/acsami.0c21365
ACS Appl. Mater. Interfaces 2021, 13, 11861−11868

forward applied bias exhibit systematic trends, as shown in Figure 4 for a sample with 10 ZnS ALD cycles (the data sets

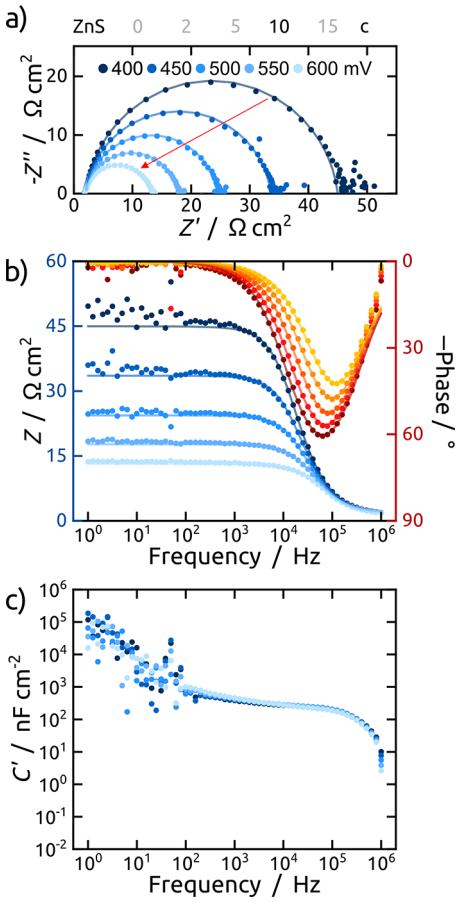

Figure 4. Trends observed by impedance spectroscopy upon varying the applied forward potential from 400 to 600 mV (direction of red arrow) under AM1.5 illumination in (a) Nyquist plot, (b) the Bode modulus (left axis) and phase (right axis) plot, and (c) the Bode capacitance plot.

collected for other configurations can be found in the SI Figures S2−S6). The device performance is perfectly stable for the duration of the measurements and current−voltage characteristics extracted from impedance spectroscopy concur with those determined by linear sweep curves (SI Figure S7c).

Samples with "thin" (≤1 nm) and "thick" (>1 nm) ZnS layers behave in contrasting manners, as presented in Figure 5 for samples with 10 and 15 ZnS ALD cycles, respectively, at 450 mV (all data are presented in the SI Figures S2−S6). While all ZnS thicknesses from 0 to 10 cycles yield a single semicircle, thicker ZnS generates more complex behavior with two overlapping characteristic time scales. All data conform to the equivalent circuit model previously developed for Sb_2S_3 solar cells.[28] It describes transport (R_{HTM}/C_{HTM}) as one limitation on the current, in series with recombination of carriers (associated with R_{rec} and the chemical capacitance C_μ). The geometric capacitance (C_{geo}) is associated with the full device structure. In our particular case, the model can be simplified given that the chemical capacitance, which is directly proportional to the density of states due to charging with minority carriers (i.e., electrons in the TiO_2 conduction band), is small in planar thin film configuration.[29,30] The data show that both transport and recombination are prevalent in the case

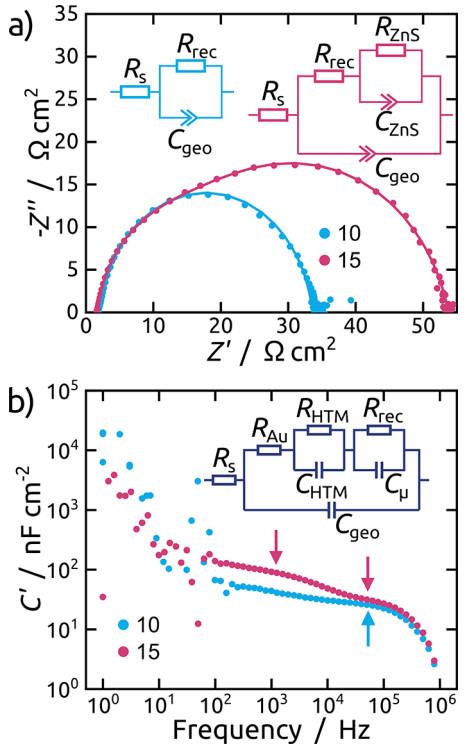

Figure 5. Impedance spectroscopic characterization of samples with "thin" and "thick" ZnS interfacial layers under AM1.5 illumination. The experimental data are presented as dots with the fitted curves overlaid as continuous lines. (a) Representative Nyquist plots for 5 and 15 ZnS cycles at an applied forward potential of 450 mV and equivalent circuit models suggested by the data: simple recombination and extraction-limited models in the "thin" and "thick" cases, respectively. (b) Bode capacitance plots, inset showing the model adapted from literature.[28]

of "thick" ZnS layers, whereas in "thin" ZnS samples no transport limitation can be discerned.[31] As an added validity check, we note that the capacitance calculated for a parallel plate capacitor equation: the ∼120 nF cm^{-2} expected of a 75 nm thick Sb_2S_3 layer (dielectric constant 14.4)[32] is in excellent agreement with the single plateau observed in the blue curve of Figure 5b, given the additional effects to be expected of the significant roughness.

The recombination resistance R_{rec} obtained for all samples depends on exponentially applied bias, as expected (Figure 6). Importantly, recombination is clearly inhibited by ZnS layers

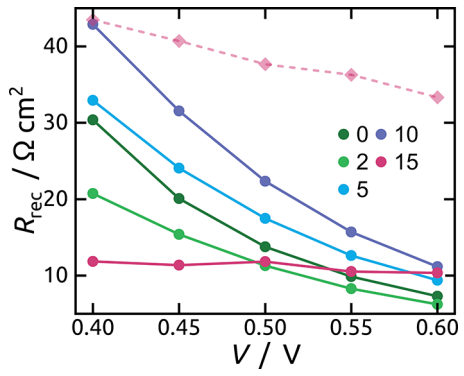

Figure 6. Evolution of the recombination resistance with the applied forward bias.

https://dx.doi.org/10.1021/acsami.0c21365
ACS Appl. Mater. Interfaces 2021, 13, 11861−11868

of increasing thickness, except for the samples treated with 2 ZnS ALD cycles. These results are in perfect agreement with the trend observed on the macroscopic scale in the overall photovoltaic power conversion efficiency and the V_{oc} up to 1.0 nm ZnS. The performance drop beyond this value, however, has already been justified by the behavior of the thick ZnS layer as an electron injection barrier determined above.

In fact, the insulating nature of ZnS also transpires in Mott–Schottky analyses, performed at 10^4 Hz (frequency identified from the C_{geo} plateau in Figure 5). The capacitance data of all

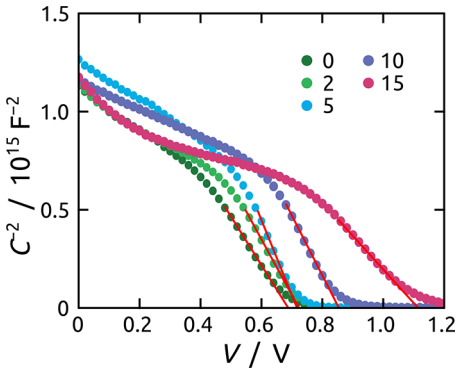

Figure 7. Mott–Schottky plots determined for different ZnS thicknesses at 10 kHz from 0 to 1.2 V. The built-in potentials are defined by the intercepts of the red lines with the *x*-axis.

cells, collected between −0.3 and +1.2 V (Figure 7), exhibits a linear section according to the following:

$$C^{-2} = \frac{2}{qA^2\epsilon N_D}(V_{bi} - V) \quad (1)$$

where q, A, ϵ, and N_D are the elemental charge, the active area, the permittivity, and the carrier density.[32,33] The built-in potential values V_{bi} determined as the intercepts with the *x*-axis increase with ZnS thickness in a monotonic manner. Even though the thickest ZnS layer seems to elicit a slightly different behavior again, which supports the previously mentioned change of dominating mechanism, the trend clearly represents an increasing junction potential achieved between TiO_2 and Sb_2S_3 by ZnS as the layer becomes increasingly continuous and thick.

Both the beneficial effect of a ZnS layer of sufficient continuity and the deleterious influence of a ZnS phase that is too thick appear in the ultrafast charge carrier dynamics of the stacks. Using transient absorption spectroscopy (TA), we can discern the three contributing rates to the photophysical evolution of n-i-p stacks: (1) charge generation and separation to the TiO_2 and P3HT layers, (2) charge back-transfer to the Sb_2S_3 layer, and (3) charge carrier recombination within the Sb_2S_3 layer.[25] The lifetimes determined by TA for reverse transfer of electrons from the TiO_2 conduction band into Sb_2S_3 are presented in Figure 8. The lifetimes increase significantly going from 2 cycles (0.2 nm) of ZnS to 5 cycles (0.5 nm) of ZnS, indicating that between those thicknesses, the ZnS layer reaches a sufficient continuity to start acting as an efficient electron blocking layer that deters reverse charge transfer. Below 5 ALD cycles, the incomplete ZnS layer rather seems to act as a recombination center. The lifetime increases further up to the 10-cycle (1.0 nm) thickness, indicating that the benefit remains. For a ZnS thickness greater than 10 cycles (1.0 nm),

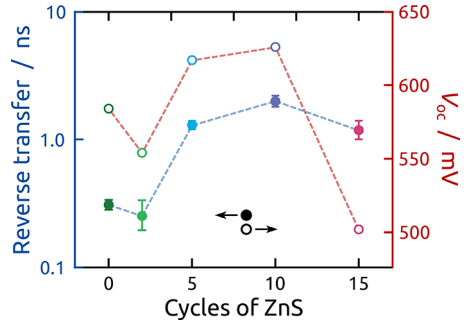

Figure 8. Time constants determined by transient absorption spectroscopy for the reverse transfer of electrons, in dependence of ZnS thickness and the corresponding champion V_{oc} values.

the lifetime of charge separation begins to decrease, indicating the deleterious effect of layers that are too thick. At this stage, the electron may remain localized in the ZnS and the lifetime that we observe is due to the reverse transfer from the ZnS interface to Sb_2S_3 rather than from TiO_2 to Sb_2S_3.[34]

Taking all the data together, the results from impedance measurements, Mott–Schottky analysis, and transient absorption measurements conspire to reveal a more complete picture underlying the PV device performance as a function of the ZnS thickness. The built-in potentials calculated from Mott–Schottky analysis (Figure 7) suggest that the ZnS interlayer formed by nanocrystallites increases its continuity from 2 ALD cycles until 10 ALD cycles (1.0 nm) are reached, further confirmed by HRTEM (Figure 2). For Sb_2S_3 solar cells without ZnS and with 2 cycles the reverse transfer lifetimes are 0.30 and 0.26 ns, respectively, being in line with literature values of cells utilizing TiO_2 substrates.[11,13,14] The trend of these charge recombination lifetimes obtained from TA spectroscopy (Figure 8) with increasing ZnS thickness is mirrored by the macroscopic parameters that define the performance of the solar cells, in particular the V_{oc} trends (Figure 8), as predicted by theoretical models..[10] The former mentioned beneficial effects of the ZnS interlayer, namely passivation and prevention of reverse electron transfer, and the converse, deleterious effect, namely prevention of forward transfer, also appear in impedance spectroscopy collected under real photovoltaic working conditions (Figure 5).

CONCLUSIONS

The defective interface between an n-type oxide and antimony sulfide as the light absorber can be stabilized chemically by a thin ZnS layer. The data presented here dissect the physical properties of this ZnS interlayer. When only one nanometer or less is present, ZnS passivates interface defects and blocks the deleterious reverse transfer of photogenerated electrons from the oxide's conduction band back into Sb_2S_3. This points to an effective way to enhance the minority carrier lifetimes and therefore, V_{oc}. In contrast to this, beyond a ZnS thickness of 1.0 nm the power conversion efficiency drops as the layer starts to behave as a barrier to electron transfer in the desired forward direction. Conversely, below 5 ALD cycles or approximately 0.5 nm nominal ZnS thickness, all investigative methods exploited here (not only the overall performance data but also Mott–Schottky curves, impedance spectroscopy, and ultrafast transient absorption) concur to indicate an increase in interfacial recombination when the ZnS layer is not continuous yet.

https://dx.doi.org/10.1021/acsami.0c21365
ACS Appl. Mater. Interfaces 2021, 13, 11861–11868

Quite surely, these conclusions hold some generality for the optimization of interfaces between oxides and heavier chalcogenide phases, which are typically a major source of efficiency losses. However, improving the interface only represents one important aspect in the quest for highly performing photovoltaics based on materials that combine the advantages of low toxicity, sufficient abundance, and processing resilience. Further limitations such as the so-called "self-trapping" in the bulk must be addressed by other means.

EXPERIMENTAL SECTION

Sample Preparation. Fluorine-doped tin oxide (FTO) substrates (Solaronix, 10 Ω/sq) were patterned by etching with HCl (2 M) and zinc powder for 10 min and then cleaned by successive sonication in detergent (Hellmanex III, 1%), acetone, isopropanol, and DI water, for 5 min each. The substrates were treated by UV-ozone cleaning for 20 min prior to further deposition steps. A hole-blocking layer of TiO_2 was spin coated from a precursor solution containing 0.255 mL titanium tetraisopropoxide (TTIP, 97 + %, Alfa Aesar) and 24 μL HCl in 3.5 mL dry isopropanol at a speed of 3000 rpm for 30 s with an acceleration of 500 rpm/s.[35] The coated samples were immediately placed onto a hot plate at 100 °C and dried for 10 min. Thereafter the samples were annealed at 500 °C for 30 min in air to convert the amorphous TiO_2 to anatase phase.

ZnS and Sb_2S_3 were deposited using a homemade hot-wall atomic layer deposition (ALD) reactor. The precursors used were diethylzinc (DEZ, 95%, abcr), tris(dimethylamido)antimony(III) ($Sb(NMe_2)_3$, 99.99%, Sigma-Aldrich), and H_2S (3% vol in N_2, Air liquide). Nitrogen was used as the carrier-gas, and the reaction temperatures were 150 and 120 °C for the deposition of ZnS and Sb_2S_3, respectively. The precursors were kept at room temperature and the opening, exposure, and pumping times were 0.2, 15, and 15 s in all cases, except for the Sb-precursor, which was opened for 1.5 s and kept at 40 °C due to the lower vapor pressure. The as-grown amorphous Sb_2S_3 layers were annealed at 300 °C for 2 min in dry inert N_2 atmosphere to convert them to the crystalline stibnite phase.

As the hole-transporting material (HTM), poly(3-hexylthiophene-2,5-diyl) (P3HT, regioregular, Sigma-Aldrich) was dissolved at a concentration of 15 mg/mL in chlorobenzene (Merck) and spin coated by injecting 50 μL on the sample spinning at 6000 rpm for 1 min. The films were dried on a hot plate for 30 min at 90 °C in dry inert N_2 atmosphere.

Thereafter, poly(3,4-ethylenedioxythiophene) polystyrenesulfonate (PEDOT:PSS, HTL Solar, Ossila) was spin coated at 6000 rpm for 60 s with an acceleration of 6000 rpm/s and again dried at 90 °C for 30 min in inert N_2 atmosphere. A gold back contact with a thickness of 100 nm was deposited by thermal evaporation (Covap evaporator, Ångstrom Engineering) using a shadow mask to define active areas of 0.12 cm^2.

Characterization. For photovoltaic characterization a solar simulator (Newport, Xe lamp source), calibrated to AM1.5 at 100 mW cm^{-2} employing a reference Si solar cell (Newport), was used. EQE spectra were recorded via an Oriel's QEPVSI-b system with a 300 W Xe light source, a monochromator and a lock-in amplifier. Electrical data was obtained by a single-channel Gamry Reference 600. A scan speed of 50 mV/s was used for *JV*-measurements from −0.3 to 1 V without any conditioning. Electrochemical impedance was measured on a Gamry Interface 1000 potentiostat under calibrated AM1.5 illumination using the solar simulator. Mott−Schottky plots were obtained in the dark at a fixed frequency of 10^4 Hz from −0.3 to 1.2 V. *JV*-curves were always recorded before and after IS and MS measurements to ensure stability of the devices. Data on sample stability are presented in SI Figure S8.

SEM micrographs were recorded using a Carl Zeiss field-emission instrument at an acceleration voltage of 2−5 kV. The cross-section transmission electron microscopy (TEM) specimen was prepared by standard lift-out technique using a ThermoFischer Helios Nanolab 660 dual beam focused ion beam (FIB)/SEM. STEM/TEM studies were performed with a (ThermoFischer) Titan[3] Themis microscope operated at 200 kV. The microscope is equipped with an ultrabright X-FEG electron source, spherical aberration correctors in both probe-forming side and imaging side. EDX elemental maps were acquired using the SuperX detector array and a high probe current. Care was taken so that the intense electron beam did not damage/alter the structure of the sample.

AFM was measured with a JPK NanoWizard 4 NanoScience AFM in tapping mode with a resonance frequency of 300 kHz.

The thicknesses of the ALD layers were determined by spectroscopic ellipsometry (SENpro, Sentech).

Samples comprised of FTO/TiO_2/ZnS/Sb_2S_3/P3HT were analyzed using transient absorption spectroscopy (TA). Excitation for TA was provided by a Coherent Libra amplified, pulsed laser system in conjunction with a Light Conversion TOPAS optical parametric amplifier. Measurements were carried out using a Helios/EOS system from Ultrafast systems. The experimental setup has been described elsewhere.[25] All samples were excited at 480 nm. For the Helios setup that acquires data over the first 5.5 ns, 250 points were obtained spaced exponentially in time and three scans were averaged. Nanosecond transient absorption (EOS configuration) data was acquired over time windows between 50 to 100 nm at randomized time delays that were also spaced exponentially. Surface Xplorer software was used for global analysis fitting by retaining 2−3 principal components and fitting 2−3 lifetimes depending on the sample configuration (2 lifetimes for ZnS/Sb_2S_3 only and 3 lifetimes for all other samples).

ASSOCIATED CONTENT

Supporting Information

The Supporting Information is available free of charge at https://pubs.acs.org/doi/10.1021/acsami.0c21365.

Figure S1, photovoltaic parameters of the solar cell devices with 0−15 cycles of ZnS; Figure S2, Nyquist, Bode phase/modulus, and Bode capacitance plots of the sample comprising a ZnS layer of 0 ALD cycles; Figure S3, Nyquist, Bode phase/modulus, and Bode capacitance plots of the sample comprising a ZnS layer of 2 ALD cycles; Figure S4, Nyquist, Bode phase/modulus, and Bode capacitance plots of the sample comprising a ZnS layer of 5 ALD cycles; Figure S5, Nyquist, Bode phase/modulus, and Bode capacitance plots of the sample comprising a ZnS layer of 10 ALD cycles; Figure S6, Nyquist, Bode phase/modulus, and Bode capacitance plots of the sample comprising a ZnS layer of 15 ALD cycles; Figure S7: Current−voltage characteristics from IS measurement data and high frequency capacitance C_{geo} for the different ZnS cycle numbers and results from equivalent circuit fitting for the sample comprising 15 cycles of ZnS for the parameters R_{rec} and R_{ZnS} and the capacitance C_{ZnS}; and Figure S8, stability tests on Sb_2S_3 solar cells: (a) performance dependence on scan speed, (b) evolution of the V_{oc} over time during illumination for the different ZnS thicknesses, and (c) *JV*-curves for solar cells employing 1 nm of ZnS fresh and after storage in a N_2-filled glovebox for 34 days (PDF)

AUTHOR INFORMATION

Corresponding Authors

Elizabeth R. Young − *Lehigh University, Department of Chemistry, Bethlehem, Pennsylvania 18015, United States;* orcid.org/0000-0002-6509-9289; Email: ery317@lehigh.edu

https://dx.doi.org/10.1021/acsami.0c21365
ACS Appl. Mater. Interfaces 2021, 13, 11861−11868

Ignacio Mínguez-Bacho − *Friedrich-Alexander University Erlangen-Nürnberg, Chemistry of Thin Film Materials, Department of Chemistry and Pharmacy, IZNF, 91058 Erlangen, Germany*; Email: ignacio.minguez@fau.de

Julien Bachmann − *Friedrich-Alexander University Erlangen-Nürnberg, Chemistry of Thin Film Materials, Department of Chemistry and Pharmacy, IZNF, 91058 Erlangen, Germany; Saint-Petersburg State University, Institute of Chemistry, 198504 Saint Petersburg, Russia;* orcid.org/0000-0001-6480-6212; Email: julien.bachmann@fau.de

Authors

Pascal Büttner − *Friedrich-Alexander University Erlangen-Nürnberg, Chemistry of Thin Film Materials, Department of Chemistry and Pharmacy, IZNF, 91058 Erlangen, Germany*

Florian Scheler − *Friedrich-Alexander University Erlangen-Nürnberg, Chemistry of Thin Film Materials, Department of Chemistry and Pharmacy, IZNF, 91058 Erlangen, Germany; Universidad de Valencia, Instituto de Ciencia de Materiales, 46980 Paterna, Spain*

Craig Pointer − *Lehigh University, Department of Chemistry, Bethlehem, Pennsylvania 18015, United States*

Dirk Döhler − *Friedrich-Alexander University Erlangen-Nürnberg, Chemistry of Thin Film Materials, Department of Chemistry and Pharmacy, IZNF, 91058 Erlangen, Germany*

Tadahiro Yokosawa − *Friedrich-Alexander University Erlangen-Nürnberg, Institute of Micro- and Nanostructure Research, and Center for Nanoanalysis and Electron Microscopy (CENEM), Erlangen 91058, Germany*

Erdmann Spiecker − *Friedrich-Alexander University Erlangen-Nürnberg, Institute of Micro- and Nanostructure Research, and Center for Nanoanalysis and Electron Microscopy (CENEM), Erlangen 91058, Germany;* orcid.org/0000-0002-2723-5227

Pablo P. Boix − *Universidad de Valencia, Instituto de Ciencia de Materiales, 46980 Paterna, Spain;* orcid.org/0000-0001-9518-7549

Complete contact information is available at: https://pubs.acs.org/10.1021/acsami.0c21365

Notes

The authors declare no competing financial interest.

■ ACKNOWLEDGMENTS

This work was supported by the European Research Council with a Consolidator Grant ("Solacylin", grant agreement 647281) and by the European Commission with a Marie Skłodowska-Curie Grant ("Hybricyl", grant agreement 795716). The NSF Major Research Instrumentation program supported the establishment of the laser facility used for transient absorption spectroscopy (CHE-1428633). We thank Profs. W. Peukert and N. Vogel for access to FE-SEM and Prof. D. Guldi for access to the AFM. F.S. stayed at Universidad de Valencia with financial support by the Erasmus+ program.

■ REFERENCES

(1) Green, M. A.; Dunlop, E. D.; Hohl-Ebinger, J.; Yoshita, M.; Kopidakis, N.; Hao, X. Solar cell Efficiency Tables (version 56). *Prog. Photovoltaics* **2020**, *28*, 629−638.

(2) Wang, W.; Winkler, M. T.; Gunawan, O.; Gokmen, T.; Todorov, T. K.; Zhu, Y.; Mitzi, D. B. Device Characteristics of CZTSSe Thin-Film Solar Cells with 12.6% Efficiency. *Adv. Energy Mater.* **2014**, *4*, 1301465.

(3) Kondrotas, R.; Chen, C.; Tang, J. Sb_2S_3 Solar Cells. *Joule* **2018**, *2*, 857−878.

(4) Mavlonov, A.; Razykov, T.; Raziq, F.; Gan, J.; Chantana, J.; Kawano, Y.; Nishimura, T.; Wei, H.; Zakutayev, A.; Minemoto, T.; Zu, X.; Li, S.; Qiao, L. A Review of Sb_2Se_3 Photovoltaic Absorber Materials and Thin-Film Solar Cells. *Sol. Energy* **2020**, *201*, 227−246.

(5) Wang, X.; Tang, R.; Jiang, C.; Lian, W.; Ju, H.; Jiang, G.; Li, Z.; Zhu, C.; Chen, T. Manipulating the Electrical Properties of $Sb_2(S,Se)_3$ Film for High-Efficiency Solar Cell. *Adv. Energy Mater.* **2020**, *10*, 2002341.

(6) Jin, X.; Fang, Y.; Salim, T.; Feng, M.; Hadke, S.; Leow, S. W.; Sum, T. C.; Wong, L. H. In Situ Growth of [hk1]-Oriented Sb_2S_3 for Solution-Processed Planar Heterojunction Solar Cell with 6.4% Efficiency. *Adv. Funct. Mater.* **2020**, *30*, 2002887.

(7) Lei, H.; Chen, J.; Tan, Z.; Fang, G. Review of Recent Progress in Antimony Chalcogenide-Based Solar Cells: Materials and Devices. *Solar RRL* **2019**, *3*, 1900026.

(8) Han, J.; Wang, S.; Yang, J.; Guo, S.; Cao, Q.; Tang, H.; Pu, X.; Gao, B.; Li, X. Solution-Processed Sb_2S_3 Planar Thin Film Solar Cells with a Conversion Efficiency of 6.9% at an Open Circuit Voltage of 0.7 V Achieved via Surface Passivation by a $SbCl_3$ Interface Layer. *ACS Appl. Mater. Interfaces* **2020**, *12*, 4970−4979.

(9) Kaienburg, P.; Klingebiel, B.; Kirchartz, T. Spin-Coated Planar Sb_2S_3 Hybrid Solar Cells Approaching 5% Efficiency. *Beilstein J. Nanotechnol.* **2018**, *9*, 2114−2124.

(10) Chen, C.; Tang, J. Open-Circuit Voltage Loss of Antimony Chalcogenide Solar Cells: Status, Origin, and Possible Solutions. *ACS Energy Letters* **2020**, *5*, 2294−2304.

(11) Yang, Z.; Wang, X.; Chen, Y.; Zheng, Z.; Chen, Z.; Xu, W.; Liu, W.; Yang, Y.; Zhao, J.; Chen, T.; Zhu, H. Ultrafast Self-Trapping of Photoexcited Carriers Sets the Upper Limit on Antimony Trisulfide Photovoltaic Devices. *Nat. Commun.* **2019**, *10*, 4540.

(12) von Hauff, E. Impedance Spectroscopy for Emerging Photovoltaics. *J. Phys. Chem. C* **2019**, *123*, 11329−11346.

(13) Christians, J. A.; Kamat, P. V. Trap and Transfer. Two-Step Hole Injection Across the Sb_2S_3/CuSCN Interface in Solid-State Solar Cells. *ACS Nano* **2013**, *7*, 7967−7974.

(14) Christians, J. A.; Leighton, D. T.; Kamat, P. V. Rate limiting Interfacial Hole Transfer in Sb_2S_3 Solid-State Solar Cells. *Energy Environ. Sci.* **2014**, *7*, 1148−1158.

(15) Deng, H.; et al. Quasiepitaxy Strategy for Efficient Full-Inorganic Sb_2S_3 Solar Cells. *Adv. Funct. Mater.* **2019**, *29*, 1901720.

(16) Chen, J.; Qi, J.; Liu, R.; Zhu, X.; Wan, Z.; Zhao, Q.; Tao, S.; Dong, C.; Ashebir, G. Y.; Chen, W.; Peng, R.; Zhang, F.; Yang, S.; Tian, X.; Wang, M. Preferentially Oriented Large Antimony Trisulfide Single-Crystalline Cuboids Grown on Polycrystalline Titania Film for Solar Cells. *Communications Chemistry* **2019**, *2*, 121.

(17) Itzhaik, Y.; Bendikov, T.; Hines, D.; Kamat, P. V.; Cohen, H.; Hodes, G. Band Diagram and Effects of the KSCN Treatment in TiO_2/Sb_2S_3/CuSCN ETA Cells. *J. Phys. Chem. C* **2016**, *120*, 31−41.

(18) Yuan, S.; Deng, H.; Yang, X.; Hu, C.; Khan, J.; Ye, W.; Tang, J.; Song, H. Postsurface Selenization for High Performance Sb_2S_3 Planar Thin Film Solar Cells. *ACS Photonics* **2017**, *4*, 2862−2870.

(19) Lee, D. U.; Woo Pak, S.; Gook Cho, S.; Kyu Kim, E.; Il Seok, S. Defect States in Hybrid Solar Cells Consisting of Sb_2S_3 Quantum Dots and TiO_2 Nanoparticles. *Appl. Phys. Lett.* **2013**, *103*, 023901.

(20) Kim, W. H.; Woo, S.; Kim, K.-P.; Kwon, S.-M.; Kim, D.-H. Efficient TiO_2 Surface Treatment Using Cs_2CO_3 for Solution-Processed Planar-Type Sb_2S_3 Solar Cells. *Nanoscale Res. Lett.* **2019**, *14*, 25.

(21) Islam, M. T.; Thakur, A. K. Two Stage Modelling of Solar Photovoltaic Cells Based on Sb_2S_3 Absorber with Three Distinct Buffer Combinations. *Sol. Energy* **2020**, *202*, 304−315.

(22) Fukumoto, T.; Moehl, T.; Niwa, Y.; Nazeeruddin, M. K.; Grätzel, M.; Etgar, L. Effect of Interfacial Engineering in Solid-State Nanostructured Sb_2S_3 Heterojunction Solar Cells. *Adv. Energy Mater.* **2013**, *3*, 29−33.

(23) Tsujimoto, K.; Nguyen, D.-C.; Ito, S.; Nishino, H.; Matsuyoshi, H.; Konno, A.; Kumara, G. R. A.; Tennakone, K. TiO_2 Surface

Treatment Effects by Mg^{2+}, Ba^{2+}, and Al^{3+} on Sb_2S_3 Extremely Thin Absorber Solar Cells. *J. Phys. Chem. C* **2012**, *116*, 13465−13471.
(24) Han, J.; Pu, X.; Zhou, H.; Cao, Q.; Wang, S.; He, Z.; Gao, B.; Li, T.; Zhao, J.; Li, X. Synergistic Effect through the Introduction of Inorganic Zinc Halides at the Interface of TiO_2 and Sb_2S_3 for High-Performance Sb_2S_3 Planar Thin-Film Solar Cells. *ACS Appl. Mater. Interfaces* **2020**, *12*, 44297−44306.
(25) Büttner, P.; Scheler, F.; Pointer, C.; Döhler, D.; Barr, M. K. S.; Koroleva, A.; Pankin, D.; Hatada, R.; Flege, S.; Manshina, A.; Young, E. R.; Mínguez-Bacho, I.; Bachmann, J. Adjusting Interfacial Chemistry and Electronic Properties of Photovoltaics Based on a Highly Pure Sb_2S_3 Absorber by Atomic Layer Deposition. *ACS Applied Energy Materials* **2019**, *2*, 8747−8756.
(26) Büttner, P.; Döhler, D.; Korenko, S.; Möhrlein, S.; Bochmann, S.; Vogel, N.; Mínguez-Bacho, I.; Bachmann, J. Solid State Interdigitated Sb_2S_3 Based TiO_2 Nanotube Solar Cells. *RSC Adv.* **2020**, *10*, 28225−28231.
(27) Platzer-Björkman, C.; Törndahl, T.; Abou-Ras, D.; Malmström, J.; Kessler, J.; Stolt, L. Zn(O,S) Buffer Layers by Atomic Layer Deposition in $Cu(In,Ga)Se_2$ Based Thin Film Solar Cells: Band Alignment and Sulfur Gradient. *J. Appl. Phys.* **2006**, *100*, 044506.
(28) Boix, P. P.; Lee, Y. H.; Fabregat-Santiago, F.; Im, S. H.; Mora-Sero, I.; Bisquert, J.; Seok, S. I. From Flat to Nanostructured Photovoltaics: Balance between Thickness of the Absorber and Charge Screening in Sensitized Solar Cells. *ACS Nano* **2012**, *6*, 873−880.
(29) Bisquert, J. Chemical Capacitance of Nanostructured Semiconductors: Its Origin and Significance for Nanocomposite Solar Cells. *Phys. Chem. Chem. Phys.* **2003**, *5*, 5360−5364.
(30) Jamnik, J.; Maier, J. Generalised Equivalent Vircuits for Mass and Charge Transport: Chemical Capacitance and Its Implications. *Phys. Chem. Chem. Phys.* **2001**, *3*, 1668−1678.
(31) Almora, O.; Zarazua, I.; Mas-Marza, E.; Mora-Sero, I.; Bisquert, J.; Garcia-Belmonte, G. Capacitive Dark Currents, Hysteresis, and Electrode Polarization in Lead Halide Perovskite Solar Cells. *J. Phys. Chem. Lett.* **2015**, *6*, 1645−1652.
(32) Ghosh, C.; Varma, B. Optical Properties of Amorphous and Crystalline Sb_2S_3 Thin Films. *Thin Solid Films* **1979**, *60*, 61−65.
(33) Abou-Ras, D.; Kirchartz, T.; Rau, U. *Advanced Characterization Techniques for Thin Film Solar Cells*; John Wiley & Sons: New York, 2016; pp 159−160.
(34) Knauf, R. R.; Kalanyan, B.; Parsons, G. N.; Dempsey, J. L. Charge Recombination Dynamics in Sensitized SnO_2/TiO_2 Core/Shell Photoanodes. *J. Phys. Chem. C* **2015**, *119*, 28353−28360.
(35) Qin, J.; Zhang, Z.; Shi, W.; Liu, Y.; Gao, H.; Mao, Y. The Optimum Titanium Precursor of Fabricating TiO_2 Compact Layer for Perovskite Solar Cells. *Nanoscale Res. Lett.* **2017**, *12*, 640 DOI: 10.1186/s11671-017-2418-9.

https://dx.doi.org/10.1021/acsami.0c21365
ACS Appl. Mater. Interfaces 2021, 13, 11861−11868